Earth Planet. Sci. Lett. 646 (2024) 118964

Contents lists available at ScienceDirect

Earth and Planetary Science Letters

journal homepage: www.elsevier.com/locate/epsl

Kinematic vorticity of shear zones that accommodate vertical crustal advection: Implications for metamorphic core complexes and pluton emplacement

Andrew V. Zuza [a,b,*], Wenrong Cao [a,c], Drew A. Levy [a,b], Joel W. DesOrmeau [a,c], Margaret L. Odlum [d], Andrew A. Siciliano [c]

[a] Nevada Geosciences, University of Nevada, Reno, NV 89557, USA
[b] Nevada Bureau of Mines and Geology, University of Nevada, Reno, NV 89557, USA
[c] Department of Geological Sciences and Engineering, University of Nevada, Reno, NV 89557, USA
[d] Scripps Institution of Oceanography, Geosciences Research Division, University of California San Diego, La Jolla, CA 92093, USA

ARTICLE INFO

Keywords:
Kinematic vorticity number
Metamorphic core complex
EBSD
Shear zone
Gneiss dome
Mylonite

ABSTRACT

Kinematic analysis of ductile shear zones is an important method to interpret the dynamic evolution of many tectonic and magmatic processes on Earth, such as orogeny, rifting, and plutonism. Despite decades of study, kinematic vorticity analysis is an underutilized tool to interpret the dynamic drivers of shear zones. Determination of the kinematic vorticity number (W_k) quantifies the relative contributions of pure- versus simple-shear strain in shear zones. Here we systematically investigated W_k from mylonitic shear zones associated with metamorphic core complexes (MCCs) developed across the central and southern North American Cordillera using electron backscatter diffraction (EBSD) data that allows consistent and reproducible results from a large number of recrystallized grains. We investigated samples from four distinct MCC systems and the structural aureole of a Cordilleran pluton to investigate their kinematics. We find that most MCC samples display pure-to-general-shear strain (average 70 % pure shear), consistent with significant bulk shear-zone shortening (>80 % shortening) observed in many of the MCC systems. Such strain patterns are remarkably similar to deformation observed around plutons that were forcefully emplaced as diapirs. To further validate and investigate these results, we constructed the W_k field of these geologic processes using numerical simulations to highlight that pure shear kinematics are more common with diapirism and coupled wallrock deformation compared with discrete detachment-involved normal fault systems. These observations support that buoyant doming can be a viable end-member process to form the investigated MCCs. Our results also suggest that pure shear deformation may be a diagnostic strain characteristic for diapir-like crustal processes, and therefore W_k analyses could be used to test similar processes like dome-and-keel models for Early Earth.

1. Introduction

Rock flow in ductile shear zones accommodates a variety of tectonic and magmatic processes. The kinematics and nature of such deformation are useful to interpret its driving dynamics. An important shear zone parameter is the relative contributions of pure shear versus simple shear (Fig. 1), which relates to whether a shear zone accommodates broad attenuation and shear-zone-normal shortening (i.e., pure shear) versus rotational strains (i.e., simple shear) that accommodate translation of rigid wallrock. As an example, interpretation of the dynamic drivers of metamorphic core complex (MCC) generation is critical for reconstructing extension across the North American Cordillera and understanding the relative contributions of vertical versus horizontal advection during MCC formation (e.g., Whitney et al., 2013). In particular, whether MCCs accommodate simple shear strain via low-angle, high-displacement normal faulting (Davis, 1983; Lister and Davis, 1989; Wernicke, 1981) or local pure shear attenuation (Miller et al., 1983) remains debated (e.g., Levy et al., 2023; Martinez et al., 2001; Tirel et al., 2008) (Fig. 2). Quantifying the kinematics of MCC shear zones can provide important insight into this debate.

* Corresponding author.
E-mail address: azuza@unr.edu (A.V. Zuza).

https://doi.org/10.1016/j.epsl.2024.118964
Received 14 March 2024; Received in revised form 30 July 2024; Accepted 25 August 2024

A quantitative parameter to characterize the relative contributions of pure shear versus simple shear is the kinematic vorticity number, W_k (Means et al., 1980) (Fig. 1). There have been numerous approaches and discussions on W_k analysis (e.g., Fossen and Cavalcante, 2017; Xypolias, 2010), but use of this parameter to directly test concrete tectonic hypotheses is rather limited (Long et al., 2019, 2016). Furthermore, the application of differing methods makes comparison of kinematic vorticity values across a geologic province challenging (Xypolias, 2010).

To advance our knowledge of shear zone vorticity and provide a practical application of vorticity analysis to quantitatively understand a geologic process, we examined the kinematic vorticity of strains related to vertical crustal advection in MCCs and pluton emplacement. We conducted vorticity analyses from several North American MCCs and use a classic Cordilleran pluton as a benchmark to test the hypothesis that MCCs formed by buoyant diapirism (e.g., Eskola, 1948) rather than detachment fault exhumation (e.g., Bartley and Wernicke, 1984; Wernicke, 1981). In addition to field geology, microstructure, and EBSD analysis, we employed 2D numerical simulations to generate W_k fields to constrain how different geologic processes result in differing W_k values. Our results reveal diagnostic strain characteristics that may be useful for evaluating ambiguous geologic processes in Earth's history or improving petrochronology approaches to date ductile deformation (e.g., Miranda et al., 2023).

2. Kinematic vorticity

Shear zones often accommodate components of both coaxial and non-coaxial strain (Fig. 1). The relative contributions of rotational flow versus pure-shear stretching are quantified via the non-dimensional W_k, which is the ratio between the vorticity tensor $\mathbf{W}$ and the stretching tensor $\dot{\boldsymbol{S}}$ components (Means et al., 1980; Truesdell, 1953). Starting with a 2D strain rate field:

$$\begin{pmatrix} \dot{\varepsilon}_{xx} & \dot{\varepsilon}_{xy} \\ \dot{\varepsilon}_{yx} & \dot{\varepsilon}_{xx} \end{pmatrix} \tag{1}$$

Means et al. (1980) defined W_k as

$$W_k = \frac{w}{\sqrt{2\Pi}} \tag{2}$$

where w is the magnitude of the vorticity vector derived from $\mathbf{W}$ and Π is the invariant second moment of $\dot{\boldsymbol{S}}$ defined as

$$\Pi = \dot{\varepsilon}_{xx}^2 + \dot{\varepsilon}_{yy}^2 + \frac{1}{2}\left[\left(\dot{\varepsilon}_{xy} + \dot{\varepsilon}_{yx}\right)^2\right] \tag{3}$$

With 2D plane strain, W_k can vary from zero, with no rotational component (i.e., pure-shear) to infinity, which is rigid-body rotation (Fig. 1A). Most geological applications of vorticity analysis assume a constant shear zone area and restrict $0 < W_k < 1$, where W_k=0 is pure shear and W_k=1 is simple shear, thus avoiding super simple shear ($W_k > 1$) and rigid-body rotation ($W_k \to \infty$) (Fig. 1A). The relationship of W_k to the pure shear component is nonlinear, and W_k=0.71 reflects equal contributions of pure shear and simple shear (e.g., Law et al., 2004) (Fig. 1B):

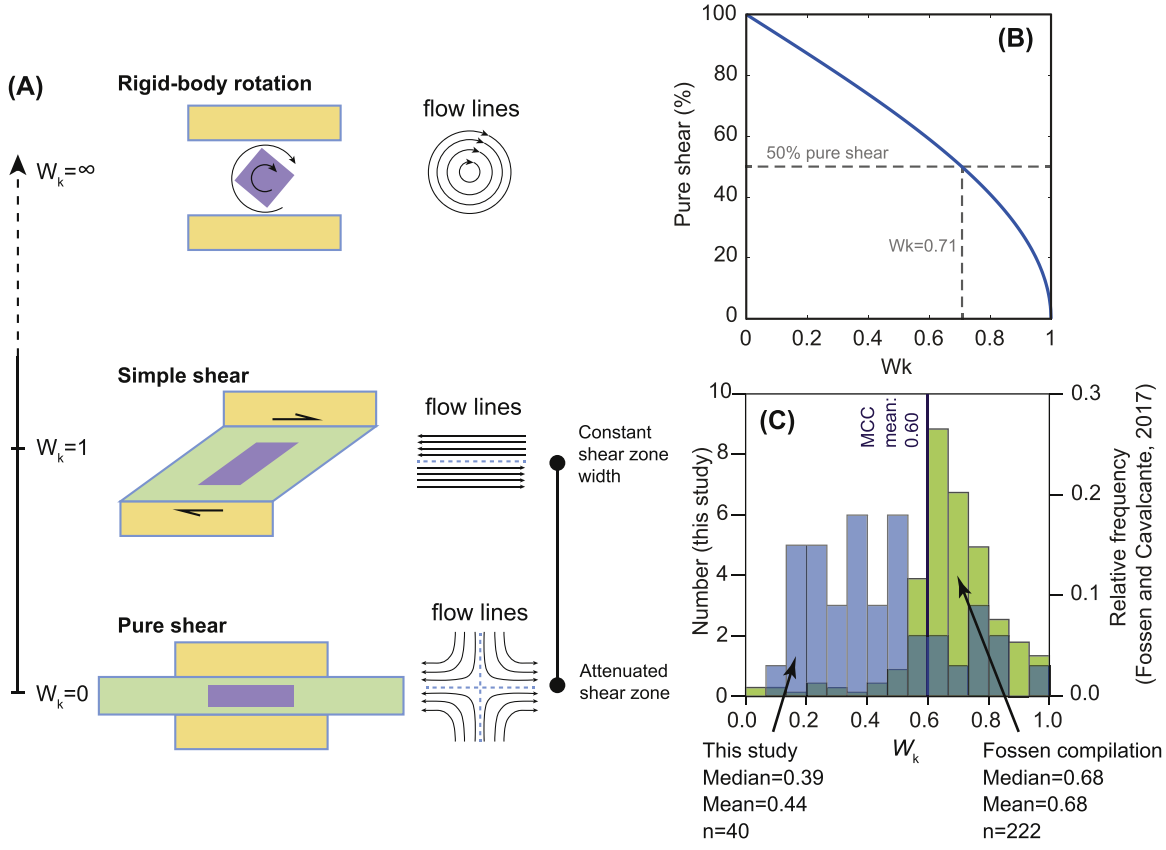

Fig. 1. Overview of kinematic vorticity number within shear zones. (A) Kinematic vorticity number (W_k) may vary from 0 (pure shear) to infinity (rigid-body rotation). For geologic shear zones, values from 0 to 1 are considered, which respectively involve attenuation or no attenuation of the shear zone width. (B) Plot showing the relationship between W_k and pure shear percentage (Law et al., 2004). The relationship is nonlinear and therefore this paper typically discusses the pure shear percentage. (C) Histogram plot showing W_k results compiled from Fossen and Cavalcante (2017) (green bars), our new generated data (blue bars), and a broad average from metamorphic core complexes (MCC) in the North American Cordillera. Note that our new data and the MCC averages are lower than the Fossen and Cavalcante (2017) compilation of mostly thrust and strike-slip shear zones, suggesting a significant difference for the MCC W_k.

$$\text{Pure shear \%} = \frac{2}{\pi}\cos^{-1}(W_k) \times 100 \quad (4)$$

Here, we quantify W_k using different microstructure-based methods on shear zone samples. Independent of W_k, the pure shear component of a shear zone can be further constrained by the attenuation of strata observed in shear zones. Simple-shear shear zones will not change their width, but the shear zone experiences vertical shortening when $W_k < 1$ (Fig. 1A). Thus, an indirect test of W_k is the bulk attenuation of a shear zone (e.g., Fossen and Cavalcante, 2017).

3. Background geology

MCCs occupy a belt that stretches along the north-south strike length of the North American Cordillera from Mexico to southwest Canada (e.g., Coney, 1980; Zuza and Cao, 2023) (Fig. 3A). MCCs formed primarily in the Cenozoic and consist of detachment faults separating upper plate rocks that are neither ductilely deformed nor metamorphosed from a metamorphosed, commonly migmatitic lower plate. Prior to their generation, east-dipping Farallon subduction beneath western North America is interpreted to have flattened and then steepened, leading to broad sweeps of late Cretaceous-Neogene volcanism (e.g., Copeland et al., 2017). This resulted in south-southwest sweeping Eocene-Oligocene volcanism from Idaho to southern Nevada and west-northwest sweeping Oligocene-Miocene volcanism across Arizona-California (Copeland et al., 2017; Humphreys, 1995). Exhumation of the MCCs associated with ductile shear zones occurred after these volcanic sweeps: exhumation of the north-central MCCs occurred in the Paleogene, with ages younging southward from Canada to southern Nevada (Whitney et al., 2013), whereas ductile exhumation of the southern MCCs occurred in the Oligocene-Miocene, younging west-northwest (Armstrong and Ward, 1991; Gans et al., 1989; Konstantinou et al., 2012; Zuza and Cao, 2023). The central MCCs were constructed in Neoproterozoic-Paleozoic passive margin strata whose original thicknesses are well documented, thus serving as benchmarks to quantify the magnitude of footwall attenuation. Central MCC footwall rocks were all strongly attenuated (>80 %) (Fig. 2D) (e.g., Lee et al., 1987; Long et al., 2023; Zuza et al., 2022). Conversely, the southern MCCs developed in orthogneiss, thus making bulk finite strain evaluations of footwall attenuation impossible.

There are two broad end-member model groups of MCC formation (Fig. 2). The MCCs may have been generated during crustal extension via detachment faulting coupled with isostatic exhumation of footwall rocks (e.g., Bartley and Wernicke, 1984; Wernicke, 1981; Wernicke and Axen, 1988) (Fig. 2A) or via the thermally induced buoyant ascent of migmatitic or plutonic cores as gneiss domes (Fig. 2C) (Eskola, 1948; Konstantinou et al., 2012; Whitney et al., 2004). Extensional detachment fault MCC models predict simple shear kinematics across the lower plate shear zones (Davis, 1983), with limited shear zone attenuation, and footwall exhumation rates comparable to plate extension rates (Fig. 2A). An alternative possible version of the detachment fault model suggests that the brittle normal fault links downdip with a diffuse zone of pure shear attenuation (Lister and Davis, 1989), which may therefore predict a mix of pure- and simple-shear strains in the ductile penetrative shear zones (Fig. 2B). Conversely, buoyant doming models predict pure shear and shear-zone-normal shortening around the rising diapir, with lower plate exhumation at rates decoupled from regional plate kinematics (e.g., Levy et al., 2023) (Fig. 2C).

Numerical simulations reveal that distinct differences in MCC style may reflect extension rates, thermal state, lower-plate viscosity, and abundance of partial melting (Rey et al., 2009). Slower extension with more partial melting leads to pure shear of the lower plate, whereas faster extension without melt favors simple shearing concentrated near the detachment fault (Rey et al., 2009). Therefore, the strain characteristics of the lower plate mylonites can help interpret MCC formation. Here we determined W_k from some Cordilleran MCCs (Fig. 3A) to better interpret their formation (Fig. 2).

We also examined the Papoose Flat pluton in the White Mountains, CA, to compare with the MCC shear zone kinematics (Fig. 3A). The ca. 83 Ma pluton was emplaced into Cambrian stratigraphy (de Saint-Blanquat et al., 2001; Sylvester et al., 1978). The host rock strata on the northwest side of the pluton are strongly attenuated >90 % (Fig. 3B) parallel with the margin of the pluton (Sylvester et al., 1978). Such attenuation is of comparable magnitude to the mylonites exposed along the central belt of MCCs (Miller et al., 1983; Wells, 2001; Zuza et al., 2022) (Fig. 3B).

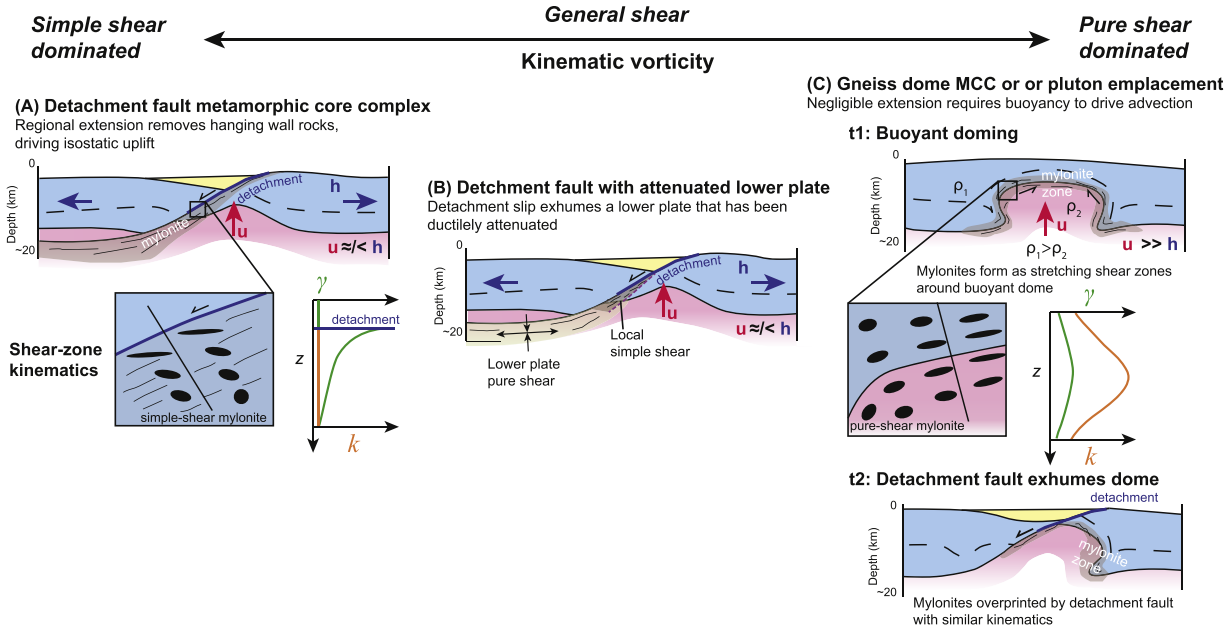

Fig. 2. Spectrum of competing end-member models for MCC development with corresponding shear zone kinematics across the shear zone (in the *z* direction), including shear strain (γ) and stretch (k). Other variables: u, vertical uplift; h, horizontal extension; ρ_1, upper-plate density; ρ_2, lower-plate density.

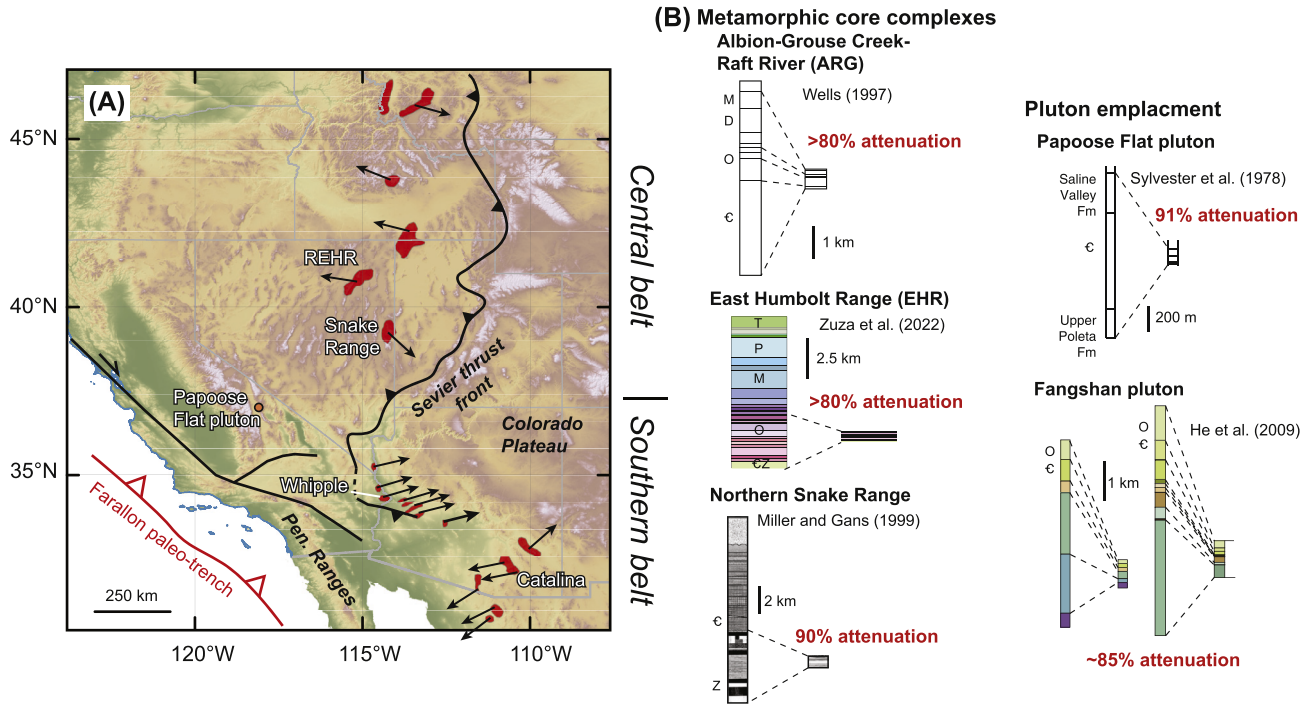

Fig. 3. (A) Map of MCCs in the North American Cordillera (labelled MCCs discussed in this work) (modified from Zuza and Cao, 2023) and (B) bulk shear zone attenuation in MCCs and pluton-emplacement shear zones. Black arrows show stretching lineation orientation in each MCC.

4. Kinematic vorticity from natural samples

4.1. Methods

Samples were collected from the Ruby Mountain-East Humboldt Range (REHR) and Snake Range MCCs in the central belt, the Whipple Mountains and Catalina MCC in the southern belt, and the northern margin of the Papoose Flat pluton (Fig. 3A). Sampling focused on collecting quartz-rich, porphyroclast-poor rocks based on our choice of vorticity methods (discussed below) and to avoid the potential impacts of porphyroclasts and/or multiphase aggregates on quartz strain geometry and rheology. Oriented thin sections were cut parallel to stretching lineations and the XZ plane for vorticity analysis. Sample location information, EBSD results, and kinematic vorticity parameters are in Table 1 and Supplemental Table S1. Sample preparation details are in the Supplemental Materials.

There are numerous methods to determine kinematic vorticity values from shear zones (Xypolias, 2010). We used electron backscatter diffraction (EBSD) datasets with a consistent MATLAB script to evaluate our samples (e.g., Levy et al, 2023) (supplied in the Supplemental Materials). EBSD analyses allowed for rapid, large area acquisitions that captured information on grain shapes, intragrain- distortion to assess grain orientation spread (GOS) and the crystallographic vorticity axis (CVA) (Michels et al., 2015), and c-axis distributions (Fig. 4). EBSD data were acquired at the University of Nevada, Reno (Zuza et al., 2022; Levy et al., 2023).

With detailed EBSD datasets (step size $\leq$20 μm), we determined quartz c-axis distributions and verified shear kinematics. Next, we primarily used the oblique grain shape foliation technique kinematic vorticity method of Wallis (1995) (referred to herein as the δ-β method) to calculate W_k:

$$W_k = \sin(2(\delta + \beta)) \quad (5)$$

where the sum of δ and β is the angle between the extensional instantaneous stretching axis (ISA_1) and shear plane. As with most kinematic vorticity methods, this approach is determining the time-averaged mean kinematic vorticity number, W_m. For consistency of terms throughout this paper, we still refer to these values as W_k. The δ and β values in a shear zone sample were calculated from the EBSD data: δ is the angle between the long axis of recrystallized quartz grains and the foliation, whereas β is the angle between the foliation and the normal of best-fit c-axis girdle (e.g., Xypolias, 2010). We determined the maximum of a kernel density estimate of the long axes of recrystallized quartz grains in polar coordinates, which is the mode. Although some studies determine the maximum δ value to approximate the ISA_1 (e.g., Sullivan, 2008; Xypolias, 2010) based on the assumption that progressive strains will rotate the long axes of neoblastic quartz grains toward the finite strain shortening plane (Wallis, 1995), we prefer to follow the approach of Long et al. (2016, 2019), who used the mean δ value. EBSD data involves many more ellipse fits (e.g., >1000) than traditional microscope-based approaches, which provides better statistics on grain orientation. The grains are deforming contemporaneously and contiguously, which makes it unlikely that newly recrystallized grains will form at different orientations (e.g., greater δ values) than neighboring grains. Experiments also suggest that the oblique recrystallized grains should maintain an approximately constant orientation during progressive strains (Dell'angelo and Tullis, 1989). We validated this assumption by calculating δ values for grains with a lower versus higher GOS from two quartzite mylonite samples from the northern Snake Range, which yielded overlapping results (Supplemental Materials). Thus, the older deformed grains (higher GOS) have not rotated relative to more recently recrystallized grains (lower GOS).

The EBSD-based δ-β method was employed over other vorticity methods for several reasons. First, this allowed us to apply the same method to samples from all study areas (Fig. 3A), while simultaneously acquiring other relevant microstructural parameters. Many of the analyzed samples were quartzite mylonites without porphyroclasts, thus limiting our use of porphyroclast-based methods (e.g., the rigid grain net, RGN method). The δ-β method captures late-stage instantaneous vorticity, which is most appropriate for studying the Cenozoic MCCs that may have experienced pre-Cenozoic deformation. Several other methods (e.g., RGN and calcite orientations) were used when applicable (see Supplemental Materials). The finite strain-β (R_{xz}-β) approach was

Table 1
New vorticity results genreated in this study.

Sample ID	Step size (μm)	Location	Latitude	Longitude	Elevation (m)	Shear sense	CVA deviation	Method	δ	β	W_k	Pure shear %	RGN[b] data		PAR[c] data	
													W_k	Pure shear %	W_k	Pure shear %
Ruby Mountains-East Humboldt Range																
AZ 10–8-19 (1a)	0.5	East Humboldt Range	40.83177	-115.14803	2251	top-west	16.8	δ-β	23	4.7	**0.82**	38.4	-	-	-	-
AZ8–19–19(4)	5	East Humboldt Range	40.95701	-115.17796	2491	top-west	15.3	δ-β	20.8	2	**0.71**	49.3	-	-	-	-
200,718–4*	5	East Humboldt Range	40.8635	-115.24592	1899	top-west	32.5	δ-β	12.3	0	**0.42**	72.7	-	-	-	-
AZ 8–4-18 (3)*	5	East Humboldt Range	40.84163	-115.13982	2193	top-west	13.5	δ-β	2.8	4.4	**0.25**	84.0	-	-	-	-
AZ 8–4-18 (1)*	5	East Humboldt Range	40.84158	-115.13997	2192	top-west	20.0	δ-β	15	0	**0.50**	66.7	-	-	-	-
020619–2*	3	East Humboldt Range	40.86344	-115.24653	1894	top-west	15.8	δ-β	1.7	4	**0.20**	87.3	-	-	-	-
AZ 6–30–20 (2)*	3	East Humboldt Range	40.94923	-115.21765	2060	top-west	6.0	δ-β	4.7	1	**0.20**	87.3	-	-	-	-
200,718–3a*	2	East Humboldt Range	40.86369	-115.24514	1901	top-west	37.0	δ-β	18.5	1.8	**0.65**	54.9	-	-	-	-
020619_5*	5	East Humboldt Range	40.864	-115.24389	1906	top-west	16.0	δ-β	15.3	8.6	**0.74**	46.9	-	-	-	-
020619–4*	2	East Humboldt Range	40.86456	-115.243	1906	top-west	18.8	δ-β	19	5.6	**0.76**	45.3	-	-	-	-
020619–3*	2	East Humboldt Range	40.86433	-115.24258	1901	top-west	20.0	δ-β	17.3	7	**0.75**	46.0	-	-	-	-
AZ 8–19–19 (2)	5	East Humboldt Range	40.95774	-115.1994	2231	top-west	10.0	δ-β, RGN	0.25	5	**0.18**	88.3	**0.51**	65.93	**0.63**	56.6
Northern Snake Range																
DL-160,619–1	2	Marble Wash	39.44601	-114.158	2044	top-east	3.5	Calcite	-	-	**0.2**	85.0	-	-	-	-
DL-160,619–3	20	Marble Wash	39.44552	-114.155	1973	top-east	20.0	Calcite	-	-	**0.5**	69.5		-	-	-
DL-160,619–5	2	Marble Wash	39.44451	-114.153	1959	top-east	15.5	Calcite	-	-	**0.5**	64.0	-	-	-	-
DL-160,619–7	2	Marble Wash	39.44432	-114.152	1921	top-east	35.5	Calcite	-	-	**0.4**	77.0	-	-	-	-
SR1	5	Hendry's Creek	39.206426	-114.07357	1781	top-east	2.2	δ-β	5	3.70	**0.30**	80.7	-	-	-	-
DL-150,619–5	3	Hendry's Creek	39.21169	-114.086	1982	top-east	5.0	δ-β	7.25	1.6	**0.30**	80.3	-	-	-	-
Papoose flat																
AZ 6–4-21(2)	10	NW Papoose Flat	-118.12796	37.029864	2494	top-north?	21.2	δ-β	6.75	2	**0.30**	80.6	-	-	-	-
AZ 6–4-21(4)	10	NW Papoose Flat	-118.12779	37.030256	2511	top-north	16	Calcite	-	-	**0.2**	90.0	-	-	-	-
AZ 6–4-21(5)	5	NW Papoose Flat	-118.12818	37.030748	2509	top-north?	21.4	δ-β	5.5	4.5	**0.34**	77.8	-	-	-	-
Whipple Mountains																
22-WD-02	5	Powerline road	34.358858	-114.28921	273	top-northeast	5.0	δ-β	12.25	1.2	**0.45**	70.1	-	-	-	-
22-WD-05	5	Powerline road	34.366742	-114.29941	329	top-northeast	4.8	δ-β	10	4.3	**0.48**	68.2	-	-	-	-
22-WD-09	5	Whipple Wash	34.329977	-114.30009	294	top-northeast	10.0	δ-β	2.5	7.9	**0.36**	76.9	-	-	-	-
AZ 3–13–22 (2)	6	Powerline road	34.380022	-114.32831	283	top-northeast	1.8	δ-β	11.5	4.2	**0.52**	65.1	-	-	-	-
AZ 3–13–22 (4)	6	Powerline road	34.376041	-114.32382	403	top-northeast	8.8	δ-β	1.25	5.75	**0.24**	84.4	-	-	-	-
AZ 3–13–22 (5)	4	Powerline road	34.375878	-114.32171	302	top-northeast	9.2	δ-β	0.75	2.8	**0.12**	92.1	-	-	-	-
AZ 3–13–22 (6)	4	Powerline road	34.36819	-114.30582	351	top-northeast	8.4	δ-β	11.25	3.2	**0.48**	67.9	-	-	-	-

(*continued on next page*)

Table 1 (*continued*)

Sample ID	Step size (μm)	Location	Latitude	Longitude	Elevation (m)	Shear sense	CVA deviation	Method	δ	β	W_k	Pure shear %	RGN[b] data		PAR[c] data	
													W_k	Pure shear %	W_k	Pure shear %
W1	10	Powerline road	34.376319	-114.32306	397	top-northeast	11.0	δ-β, RGN	2.25	7.5	**0.33**	78.3	**0.68**	52.83	**0.59**	59.8
Catalina																
AZ 2–10–23(3)	7	Molino Basin	32.340647	-110.73182	1505	top-northeast	12.3	δ-β	1.5	3.1	**0.16**	89.8	-	-	-	-
AZ 2–10–23(4)	8	Molino Basin	32.337879	-110.68514	1423	top-northeast	33.8	δ-β	3.5	3.5	**0.24**	84.4	-	-	-	-
AZ 2–12–23 (3)	5	Tanque Verde	32.252361	-110.66196	872	top-southwest	1.3	δ-β	0.25	6.8	**0.24**	84.3	-	-	-	-
AZ 2–8-23(2)	4	Babad Do'ag	32.311506	-110.71676	1141	top-southwest	13.0	δ-β	21	6.9	**0.83**	38.0	-	-	-	-
AZ 2–8-23(7)	5	Laramide(?) structure	32.455109	-110.78366	2498	top-northeast	35.5	δ-β	6	48	**0.95**	20.0	-	-	-	-
AZ 2–10–23 (2)	-	Molino Basin	32.34882	-110.74705	1337	top-northeast	-	RGN	-	-	-	-	**0.52**	65.2	**0.46**	69.6
AZ 2–10–23 (6)	-	Molino Basin	32.337901	-110.68305	1476	top-northeast	-	RGN	-	-	-	-	**0.4**	73.8	**0.59**	59.8
AZ 2–10–23 (8)	-	Molino Basin	32.342318	-110.68386	1391	top-northeast	-	RGN	-	-	-	-	**0.32**	79.3	**0.41**	73.1
AZ 2–8-23 (5)	-	Babad Do'ag	32.367711	-110.71863	2007	top-southwest	-	RGN	-	-	-	-	**0.32**	79.3	**0.41**	73.1

[*] Data from Levy et al. (2023)
[b] Rigid-grain net
[c] Porphyroclast aspect ratio

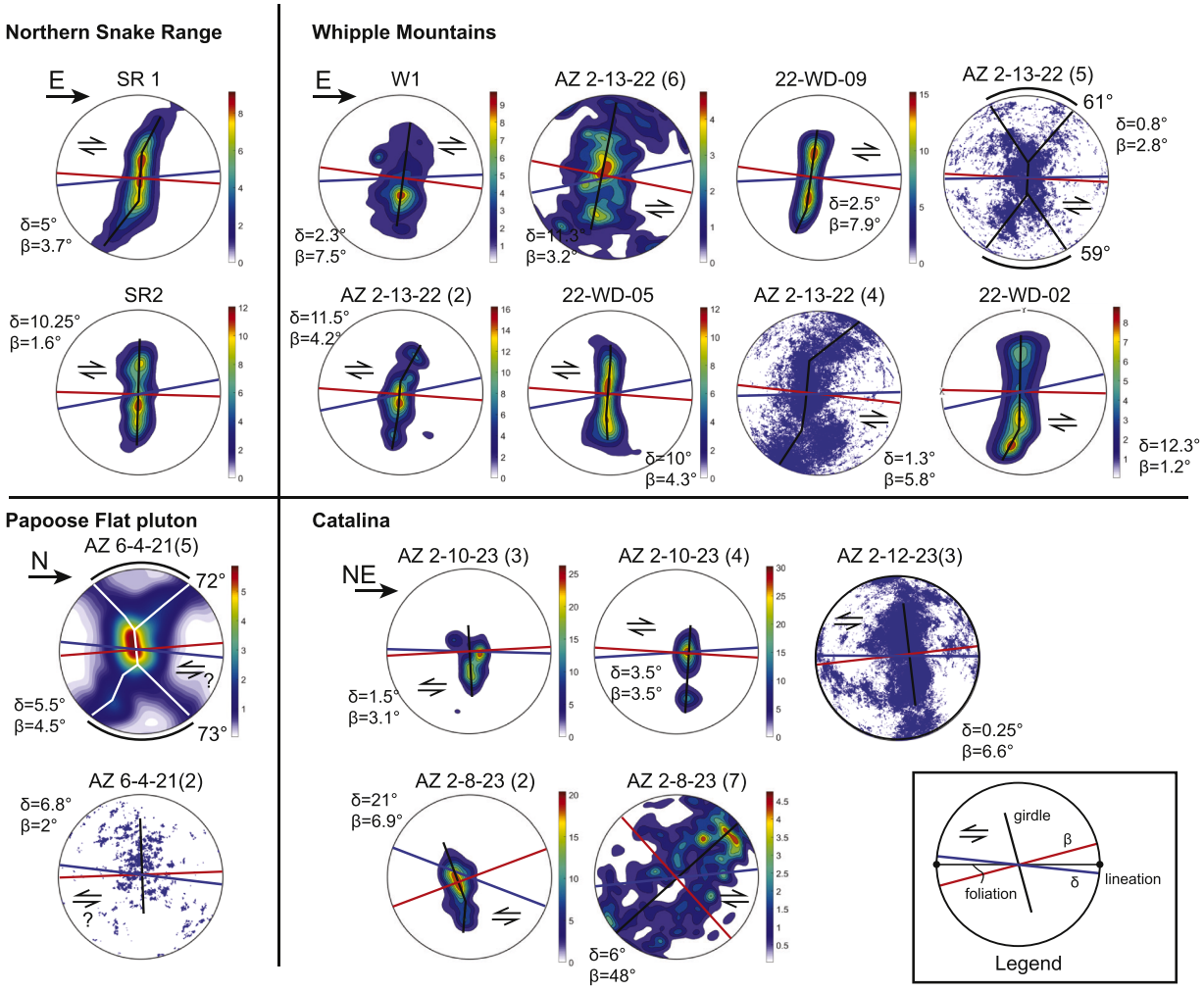

Fig. 4. Overview of EBSD data from newly analyzed samples, including kinematic vorticity parameters. Lower-hemisphere pole figures from each sample are shown, along with the β and δ fits. Most pole figures show contoured c-axis data, and a few show point scatter or orientation distribution functions (ODF) because they better conveyed the orientation of the c-axis girdle. Interpreted kinematics based on the EBSD data and petrographic observations. Sample data was flipped to keep geographic orientations consistent among samples from the same location. Opening angles were determined for thermometry for samples that displayed a cross-girdle c-axis distribution.

not used because such strain-based approaches may be less robust due to the sensitivity to β value and reliance on finite strain estimates (e.g., Xypolias, 2010), which are problematic due to the (1) fine recrystallization of many of the mylonite samples and (2) potential for polyphase deformation in many MCCs.

Estimates of the δ and β angles are only valid if the thin section is cut perpendicular to the kinematic vorticity axis (Díaz-Azpiroz et al., 2019), in which case the thin section should present the vorticity normal section (VNS). To validate this, we employed CVA analyses (Michels et al., 2015) for all analyzed samples. We calculated the deviation of the CVA axis from the sample Y-axis, C_Y, which is represented by the center of the stereonet plot (Fig. 5B).

4.2. Results

In the REHR, new vorticity data was collected to supplement existing data published in Levy et al. (2023). The ~1-km-thick REHR mylonitic shear zone developed within Proterozoic-Paleozoic passive margin stratigraphy and Mesozoic-Cenozoic intrusions. This shear zone vertically attenuates the stratigraphy >80 % (Fig. 3B). Quartzite samples and one deformed Oligocene granite were collected from the shear zone on the western flank of the East Humboldt Range with WNW-trending lineations (Levy et al., 2023; Zuza et al., 2022) (Fig. S1 in the Supplemental Materials). All samples display top-WNW shear sense (Fig. S6 in the Supplemental Materials)—determined via mica fish and asymmetric mantled porphyroclasts—and consist of recrystallized quartz that deformed at ~400–600 °C as determined via Ti-in-quartz thermometry (Levy et al., 2023) (Supplemental Table S1). CVA analyses confirmed that samples were cut parallel to the VNS with most samples yielding C_Y values <20° (Fig. 5B). C-axis girdles were inclined gently west with β of 0–8.6° Best-fit ellipses on quartz grains showed long axes stretched northwest with δ values of 1.7–20.8° The resultant W_k values spanned 0.18–0.82 (88–38 % pure shear), with an average of 0.51 (Fig. 5A). Rigid-grain analyses from the deformed granite sample yielded W_k of 0.51–0.63 (66–57 % pure shear) (Fig. 5A).

The northern Snake Range shear zone vertically attenuates Proterozoic-Paleozoic passive margin stratigraphy by ~90 % (Fig. 3B) (Lee et al., 1987; Long et al., 2023; Miller et al., 1983). We analyzed two quartzite and four calcite-marble mylonite samples, collected from the eastern flank of the range (Fig. S2 in the Supplemental Materials). Lineations trend east and deformation kinematics are top-east from mica fish and asymmetric calcite grains (Fig. S6 in the Supplemental Materials). Sample SR1 displayed a weak cross-girdle geometry in a scatter plot of c axes (Supplemental Materials), which was used to calculate an opening-angle thermometry deformation temperature of ~482 ± 50 °C (Supplemental Table S1) using the Faleiros et al. (2016) calibration.

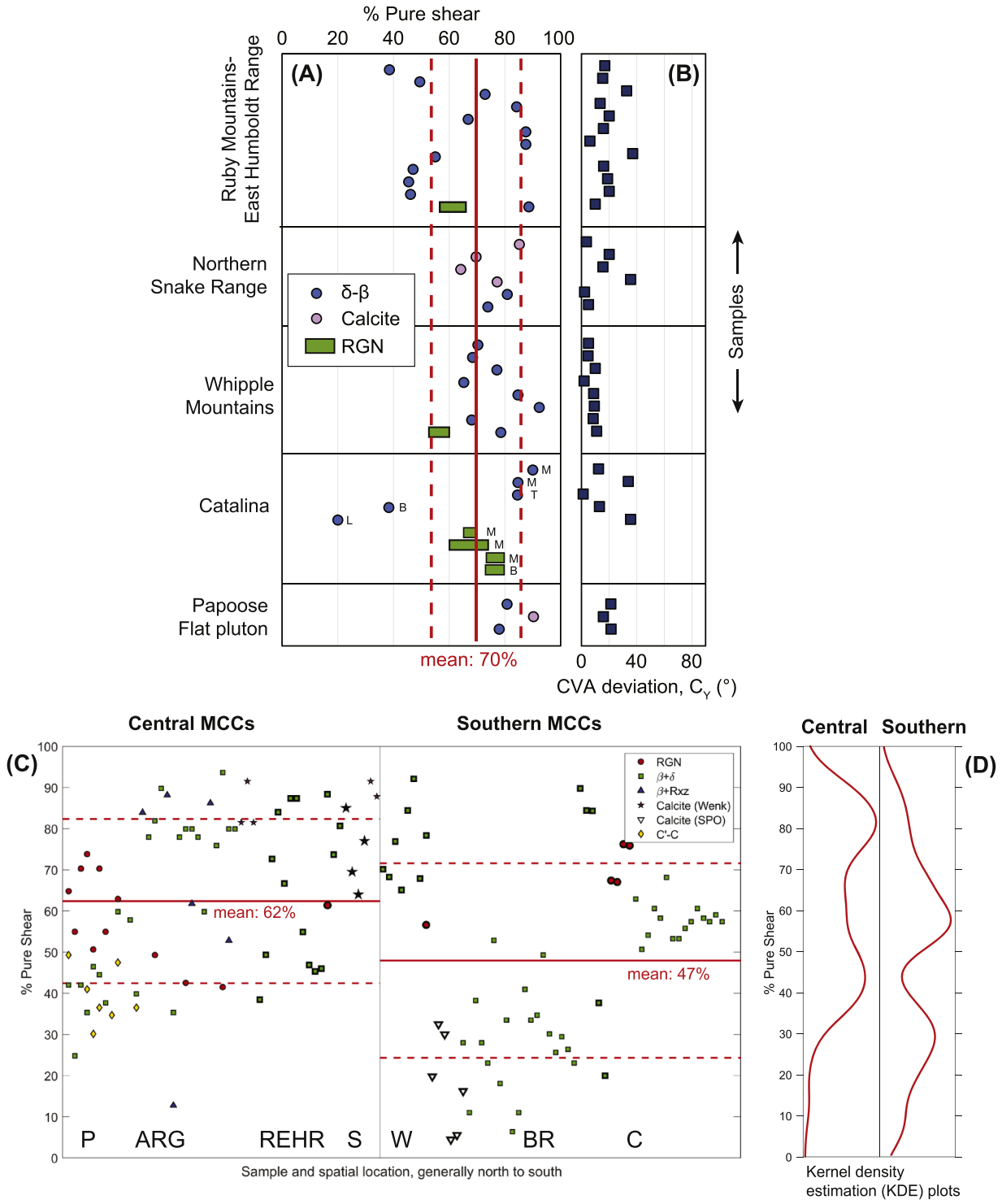

Fig. 5. (A) Plot of kinematic vorticity results from this study, including data from Levy et al. (2023) from the Ruby Mountains-East Humboldt Range. RGN is rigid grain net. For the Catalina samples, shear zone location information is provided and discussed in the text: M—Molino Basin, T—Tanque Verde, B—Babad Do'ag, and L—Laramide(?) structure. (B) Plot of the deviation angle of the crystallographic vorticity axis (CVA) and sample Y axis, C_Y. (C) Compilation of kinematic vorticity number results from the North American metamorphic core complexes (MCCs), including new results from this study. Samples are generally arranged from north (left) to south (right). Locations: P—Pioneer; ARG—Albion-Raft River-Grouse Creek; REHR—Ruby Mountain-East Humboldt Range; S—Snake Range; W—Whipple; BR—Buckskin-Rawhide; C—Catalina. (D) Kernel density estimates for the central and southern MCCs showing a moderate bimodal distribution.

CVA C_Y values for the quartzite samples were <5° and for the calcite samples were more variable at 3.5–35.5° (Fig. 5B). In the quartzite mylonites, c-axis girdles were inclined east with β values of 1.6–3.7° The δ values spanned 5–10.25° These values yield W_k values of 0.3–0.4 (81–74 % pure shear) (Fig. 5A). In the calcite marbles, the inclined c-axes suggest W_k values of 0.2–0.5 (85–64 % pure shear) (Fig. 5A).

The mylonitic footwall of the Whipple Mountains detachment fault system consists of Proterozoic orthogneiss intruded by Mesozoic-Cenozoic intrusions. The shear zone does not have reliable indicators for the magnitudes of vertical attenuation. We collected and analyzed eight samples from the northeast part of the Whipple Mountains (Fig. S3 in the Supplemental Materials). Stretching lineations trend northeast and all observed fabrics suggest top-northeast shear (Fig. S6 in the Supplemental Materials). We analyzed eight quartz-rich orthogneiss and schist samples. All showed CVA C_Y ≤11° (Fig. 5B). Opening angle thermometry from two samples confirmed deformation at temperatures of ~450 ± 50 °C (Supplemental Table S1) (Faleiros et al., 2016). Samples yielded c-axis girdles that were inclined to the northeast with β values of 1.2–7.9° The δ values spanned 0.75–11.25° These values yield variable but pure shear dominated W_k values of 0.12–0.50 (92–67 % pure shear) (Fig. 5A; Table 1). Rigid-grain analyses from one porphyritic orthogneiss sample yielded W_k of 0.59–0.68 (60–53 % pure shear) (Fig. 5A).

The Catalina MCC involves deformed Proterozoic and Mesozoic-Cenozoic plutons, with no reliable indicators of vertical attenuation. Five samples were collected and analyzed for δ-β-based W_k analyses and four samples for rigid-grain W_k analyses. Sampling focused on several distinct shear zones in the Catalina Mountains, including the top-southwest Babad Do'ag and Tanque Verde shear zones on the western flank of the range, the top-northeast Molino Basin shear zone within the range interior (Spencer et al., 2022), and the top-east shear zone exhumed from beneath the MCC mylonites that are interpreted to represent older (Late Cretaceous-Eocene) Laramide structures (Bykerk-Kauffman and Janecke, 1987) (Figs. S4 and S6 in the Supplemental Materials). Most CVA results from the Catalina samples show little deviation (<15°) from C_Y. However, the two samples that displayed some of the highest C_Y values at 33–35° (Fig. 5B) were from the top-northeast-east shear zones (i.e., Molino Basin and Laramide) that may have experienced complex kinematics.

The top-southwest Babad Do'ag and Tanque Verde shear zones showed a mix of kinematic vorticity results with W_k values from 0.24–0.83 (84–38 % pure shear) (Table 1). The top-northeast Molino Basin shear zone yielded fairly low W_k values from the δ-β and rigid-grain methods of 0.16–0.57 (90–61 % pure shear) (Table 1). Lastly, the Laramide-aged (Late Cretaceous-Eocene) shear zone showed top-east simple shear kinematics (W_k = 0.95; 20 % pure shear) (Table 1).

Finally, for the Papoose Flat pluton, two quartz-rich samples and one calcite marble from the strongly attenuated (Fig. 3B) northwestern country rock were analyzed (Fig. S5 in the Supplemental Materials). The quartzose samples yielded W_k values of 0.30–0.34 (81–78 % pure shear) at temperatures of ~550 °C based on OA thermometry (Table 1 and S1; Figs. 4 and 5A). The analyzed calcite marble had a c-axis girdle that was <5° from vertical, which suggests >90 % pure shear (Wenk et al., 1987) (Fig. 5A).

5. Kinematic vorticity from numerical models

5.1. Methods

Numerical simulations were conducted to examine kinematic vorticity using the MATLAB-based MVEP2 thermo-mechanical modeling package (Kaus, 2010). The code uses nonlinear viscous flow laws (e.g., Ranalli, 1995). Simulations were conducted using either fixed rheological conditions or variable conditions that involve temperature-varying density and partial melting based on *P-T* conditions. The primary output results used in this work was the velocity field ($\vec{v}$). The 2D vorticity is the curl of $\vec{v}$, defined:

$$vorticity = \nabla \times \vec{v} = \left(\frac{\partial v_y}{\partial x} - \frac{\partial v_x}{\partial y}\right)\hat{\mathbf{k}} \tag{6}$$

where v_y and v_x are the velocity in the vertical and horizontal directions, respectively. The vorticity vector has the unit of s^{-1} and is the out-of-plane direction of $\hat{\boldsymbol{k}}$. The magnitude of vorticity describes the rotational nature of the flow, and the sign of the vorticity indicates the spin direction, with positive being counterclockwise. W_k can be calculated using Eq. (2) (Means et al., 1980; Tikoff and Fossen, 1995) to include the velocity field:

$$W_k = \frac{\frac{\partial v_y}{\partial x} - \frac{\partial v_x}{\partial y}}{\sqrt{2\left(\frac{\partial v_x}{\partial x} + \frac{\partial v_y}{\partial y} + \frac{1}{2}\left(\frac{\partial v_x}{\partial y} + \frac{\partial v_y}{\partial x}\right)^2\right)}} \tag{7}$$

Since W_k generated in the numerical simulation is relative to a Eulerian grid in the model, which is an external reference frame and contains a component of rigid-body rotation, its absolute value can significantly exceed 1. To generate W_k values that are comparable to geological observations ($0 < W_k < 1$), we did not calculate W_k for regions where the internal strain rate was significantly lower than the background strain rate to focus on the "internal kinematic vorticity" of discrete shear zones that might be observed in geologic outcrops (Tikoff and Fossen, 1995). To evaluate rotation direction, we allow $-1 < W_k < 1$. We convert W_k to percentage of simple shear in the plots because the nonlinear nature of W_k (Fig. 1B) can be visually misleading (i.e., W_k >0.71 is > 50 % simple shear).

Benchmark tests involving 0 %, 50 %, and 100 % pure shear validated the applicability of our numerical approach (Fig. S38 in the Supplementary Materials). The pure shear models generated a homogenous $W_k = 0$ field, the simple shear models generated a homogenous $W_k = 1$ field, and models with equal parts simple- and pure-shear strain rates resulted in a homogenous W_k = 0.71 field (Fig. S38 in the Supplementary Materials).

We conducted three sets of numerical experiments. First, we generated a buoyant diapir with fixed density and viscosity conditions to approximate a rising pluton or diapiric dome. Second, we generated a gneiss dome driven by basal heating and partial melting. Finally, we simulated regional extension with a weak seed fault, which resulted in a detachment-fault-type MCC.

5.2. Results

Following the benchmark simulations, the first set of numerical models involved a lower density (2600 kg/m^3 fixed 10^{18} Pa s viscosity) circular feature that buoyantly rose within the host rock (2800 kg/m^3 density) with a wet quartzite power law rheology (Ranalli, 1995) (~10^{19}–10^{21} Pa s viscosity). The size and density of the diapir did not impact the broad patterns of W_k (Figs. S39 and S40 in the Supplemental Materials). The diapir rose rapidly in these simulations surrounded by a rim of pure shear (Fig. 6). The rising diapir generated two regions of extreme rotation along its flanks, where the rocks flowed downward and under the diapir (Fig. 6A). This resulted in local high W_k values due to the rotational flow around the diapir. The lower strain rates with high velocity in these domains suggests rigid-body rotation, hence greater W_k values. A profile across the top of the rising circle shows W_k values near 0 % simple shear that varied up to ~25 % simple shear with both clockwise and counterclockwise rotations (Fig. 6B).

In the next simulation, the base of the crust was fixed at 800 °C to drive partial melting and diapirism (Fig. 7). This model generated three distinct diapirs that rose from the base of the model. Each diapir was rimmed by wallrock that experienced mostly pure shear strain, although

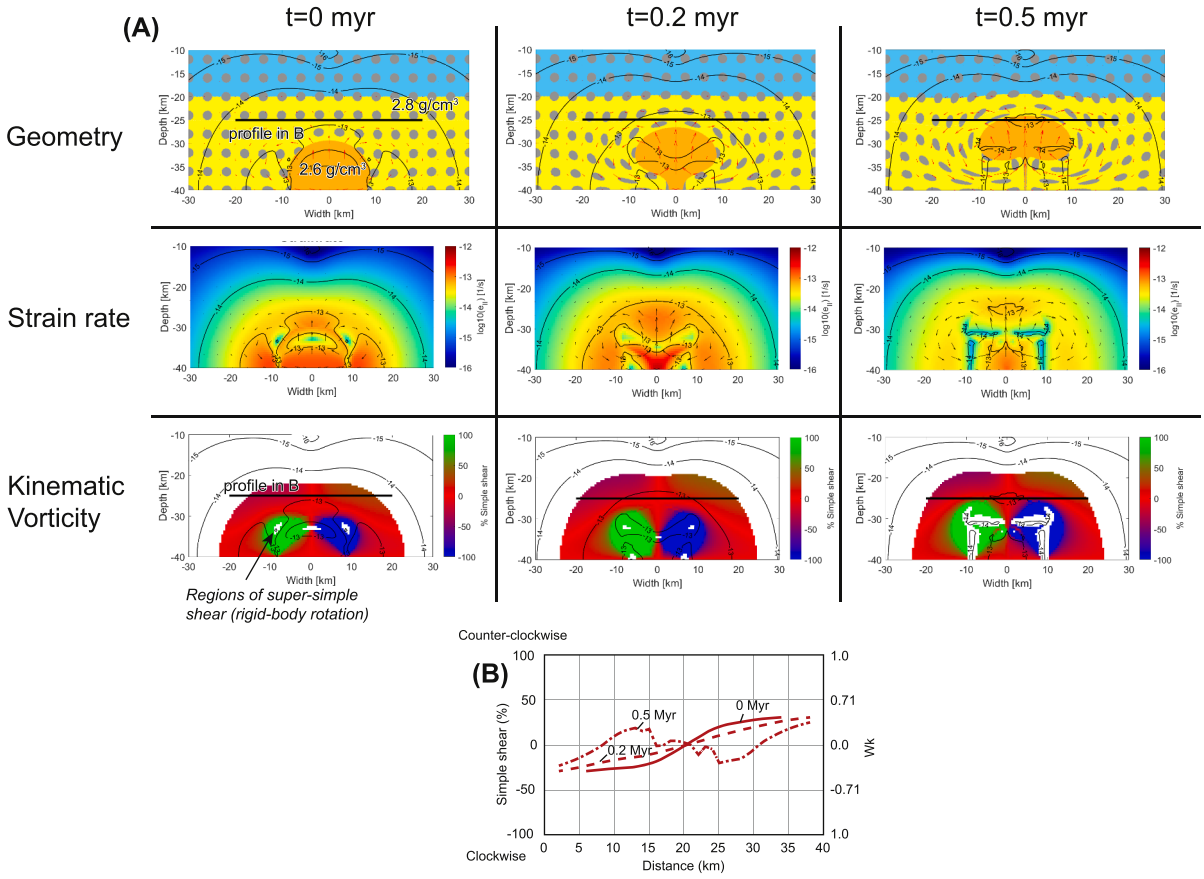

Fig. 6. Simulation of a less dense sphere rising in a denser medium. (A) Graphical summary of results after 0, 0.2, and 0.5 Myr, including geometry, strain rate, and kinematic vorticity. Coloring is only to display kinematics and does not imply differing rheology. Note regions of rigid body rotation (super simple shear) along the flanks of the rising body. (B) Profile plot of kinematic vorticity vs distance for the three time intervals, based on the black-line profile in A. Note the y axis in B is simple shear percent. Gray dots are passive strain makers. Blue and yellow crust have the same properties and are merely used to differentiate upper vs mid-lower crust.

there were very distinct regions of significant rotation around the edge of the riding diapir head. These rotating regions yielded W_k values >>1 and experienced rigid-body-like rotation. For a diapiric gneiss dome, the main mylonitic shear zones would form where strain rates are relatively high on top and marginal flanks of the rising diapir head. Therefore, we examined the kinematic vorticity values directly above and to the sides of these diapirs. The gneiss dome models generated W_k values that were mostly near 0 (0 % simple shear) (Fig. 7). There were some regions where simple shear strain was significant, which was where the rising diapir caused the wallrock to rotate around the diapir head (Fig. 7).

To simulate extensional detachment-fault-style MCCs, we conducted a series of numerical models that included horizontal stretching of the model domain (10^{-14} s^{-1} strain rate) (Fig. 8). The models involved a single temperature-dependent wet quartzite rheology with an inclined weak seed to initially focus upper-crustal faulting along a single detachment fault system (Rey et al., 2009). These models resulted in inclined discrete shear zones with the upward flow of a middle core. The highest strain rates (10^{-12}–10^{-13} s^{-1}) focused in the upper-mid crust shear zones. These shear zones were markedly different from the first series of diapir models in that they displayed predominately (>50 %) simple shear strain (Fig. 8).

Corollary experiments with varying diapir size, density, strain rates, and one model with contractional boundary conditions resulted in similar kinematic vorticity values when compared to our reference models (Figs. 6-8) (Supplemental Materials). Contractional boundary conditions generated a major reverse shear zone with simple shear kinematics (Supplemental Materials).

6. Discussion

6.1. Kinematic vorticity estimates

Most of the samples had C_Y values $\leq 20^\circ$ (27 of 34 samples), confirming that our analyses were performed within the VNS (Fig. 5B). Our new vorticity results yielded an average of 70 % pure shear (±16 %) (Fig. 5A). Average results from the rigid grain methods (67 % pure shear) were similar to the δ-β method (~70 % pure shear), which provides confidence in our approach. There is no discernable trend in the data for significant variations of W_k for differing MCCs (Fig. 4A). Vorticity results from the MCC samples (average 69 % pure shear) are similar to, but slightly lower, than those from the Papoose Flat pluton (83 % average pure shear).

The Catalina MCC yielded the most diverse W_k estimates from the analyzed samples (Fig. 5A). This diversity correlates with the variety of shear zone kinematics inferred within the Catalina MCC system, including MCC-age shear zones with varying kinematics and interpreted Laramide structures (Bykerk-Kauffman and Janecke, 1987). The older Laramide structures are found at deep structural levels within the Catalina MCC, and have variable east-directed shear sense with both older-on-younger and younger-on-older juxtaposition relationships (Bykerk-Kauffman and Janecke, 1987). In this sense, variable shear zone kinematics are expected because each shear zone may have involved a differing finite strain history.

Our vorticity analyses can be compared against external geological constraints. Attenuated stratigraphy within the central MCCs requires significant shear-zone-normal shortening during deformation (Fig. 3B),

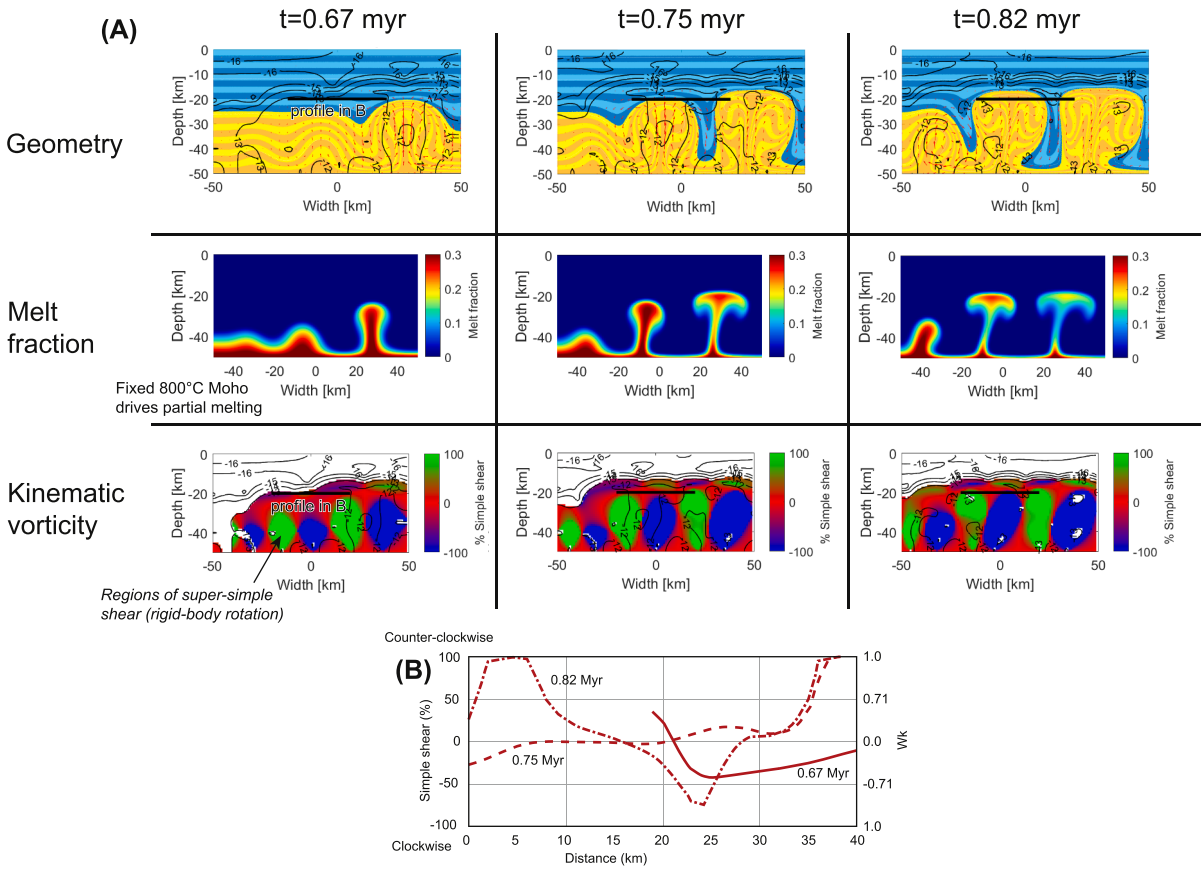

Fig. 7. Temperature dependent rheology and partial melting simulation of positively buoyant diapirs. A fixed 800 °C bottom boundary condition drives partial melting. (A) Graphical summary of results after 0.67, 0.75, and 0.82 Myr, including geometry, melt fraction, and kinematic vorticity. Note regions of rigid body rotation (super simple shear) along the flanks of the rising diapirs. (B) Profile plot of kinematic vorticity vs distance for the three time intervals, based on the black-line profile in A. Note the y axis in B is simple shear percent. Gray dots are passive strain makers. Blue and yellow crust have the same properties and are merely used to differentiate upper vs mid-lower crust.

which thus implies a significant component of pure shear strain. A simple-shear shear zone will maintain a constant width, whereas a pure-shear shear zone is vertically shortening and horizontally stretched (Fig. 1A). Therefore, the attenuation observed in the REHR, northern Snake Range, and Papoose Flat shear zones independently confirms a significant pure shear component to deformation that matches our W_k observations with >50 % pure shear for most samples. The southern MCCs do not have external constraints for shear zone attenuation, but the similar W_k values (Fig. 5) suggests they may have involved significant attenuation.

Compared to a global synthesis of predominately strike-slip and thrust shear zones, our results demonstrate that the MCC and pluton emplacement fabrics had significantly lower W_k values: our results had a median W_k of 0.39 versus Fossen and Cavalcante (2017)'s synthesis median of 0.68 (Fig. 1C). These differences imply that differing deformation regimes may intrinsically develop distinct shear zones.

The numerical simulations of buoyant diapirs suggest predominately pure shear deformation (>70 % pure shear) around the tops and sides of the rising domes (Figs. 6 and 7). Regions of super simple shear are found along the edges of the rising diapirs, where material flows around the edge of the diapir/domes. We argue the curviplanar rims of the rising diapir in the numerical models are most similar to the natural mylonitic shear zones examined in this work, which usually have a subhorizontal fabrics and exist as a shear zone carapace above a more ductilely deformed metamorphic infrastructure (e.g., Snoke, 1980). Therefore, the numerical simulations predict predominately general-shear to pure-shear deformation around diapir-driven deformational systems. In simulations with discrete shear zones akin to a discrete detachment faults, more simple shear kinematics were observed (Fig. 8). In these experiments, shear strains were concentrated in a weak shear zone, which effectively allowed rigid hanging wall and footwall rocks to shear past each other in a simple-shear shear zone.

6.2. Implications for metamorphic core complexes

MCC formation mechanisms can be tested via the W_k values of MCC-bounding shear zones (Fig. 2). Our results show that the MCC shear zones deformed via general shear (~69 % pure shear). Compiled vorticity data (Erskine et al., 1993; Levy et al., 2023; McFadden et al., 2020; Singleton, 2011; Singleton et al., 2018; Sullivan, 2008; Yun, 2018) from the North American MCCs, filtered for similar methods (Supplemental Materials), shows a broad pattern of general shear (Fig. 5C). The central MCCs show more pure shear strain (62 %) than the southern MCCs (47 % pure shear) (Fig. 5C). In detail, both domains reveal a moderate bimodal distribution (Fig. 5D). The Cordillera-wide mean values show 56±23 % pure shear, which overlaps the vorticity results from this study (i.e., 70±16 %) within uncertainty. Therefore, available results demonstrate that the North American MCC footwall rocks experienced general shear.

General-to-pure shear strain of the lower plate mylonites is not consistent with the traditional detachment fault model for MCC generation (Fig. 2A). If brittle detachment faulting was directly linked with penetrative ductile shearing at depth, we would expect simple-shear-dominated fabrics that accommodate significant hanging wall translation. Instead, these general shear strain characteristics may support one of two scenarios. First, the lower-plate mylonites may accommodate

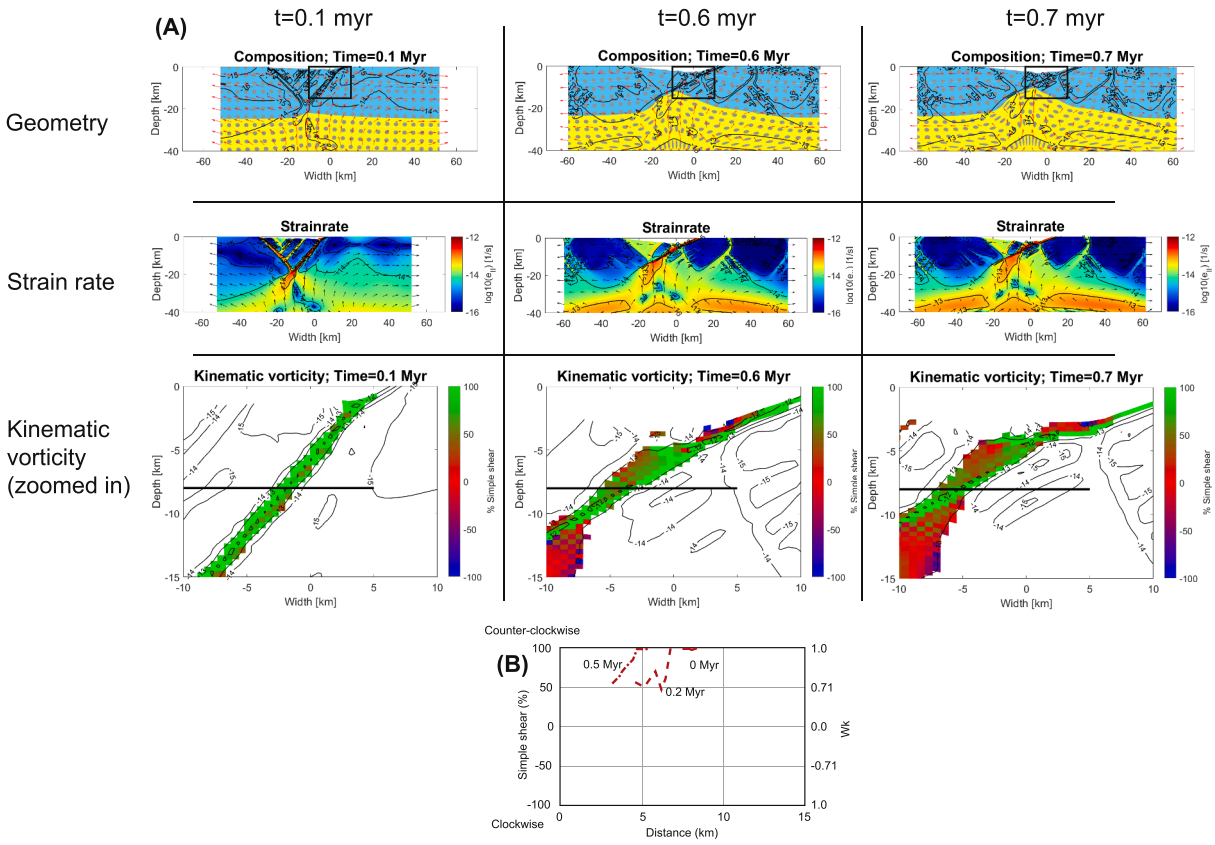

Fig. 8. Simulation involving a weak initial shear zone to create a detachment-fault type metamorphic core complex. (A) Graphical summary of results after 0.1, 0.6, and 0.7 Myr, including geometry, stain rate, and kinematic vorticity zoomed into the black-box region in the top row. (B) Profile plot of kinematic vorticity vs distance for the three time intervals, based on the black-line profile in A. Note the y axis in B is simple shear percent. Gray dots are passive strain makers. Blue and yellow crust have the same properties and are merely used to differentiate upper vs mid-lower crust.

bulk attenuation downdip of a master detachment fault during regional extension (Lister and Davis, 1989). In this case, regional crustal extension may lead to ductile stretching of the lower plate that kinematically linked upward with synchronous normal faulting in the upper crust (Fig. 2B). Alternatively, gneiss dome diapirism may have attenuated the surrounding wallrock to form the general shear mylonites (Zuza et al., 2022; Levy et al., 2023) (Fig. 2C). Such crustal diapirs would have stalled in the upper crust, thus requiring later normal faults to exhume the ductile fabrics (Fig. 2C).

The geology of the central MCC belt can differentiate between these competing models. Here, Oligocene mylonites (e.g., Lee et al., 2017; Zuza et al., 2022) were temporally decoupled from Miocene detachment faulting associated with regional extension across the Great Basin (e.g., Colgan and Henry, 2009). Oligocene shearing did not generate syn-kinematic basins of substantial thickness (Konstantinou et al., 2012; Zuza et al., 2022), whereas Miocene extension generated widespread, thick syn-tectonic basins (e.g., Henry et al., 2011). The traditional detachment fault models (Fig. 2A and B) require a brittle normal fault to break the surface at the time of ductile shearing, and the lack of evidence for surface-breaking normal faulting tracked via low-temperature thermochronology or syn-kinematic basin sedimentation (see Zuza and Cao, 2023 for a review) is at odds with these models.

The gneiss dome model predicts that lower plate MCC exhumation should correspond to a time of lower crust heating and partial melting to drive crustal diapirism. This model suggests that the crust was heated during post-flat-slab rollback, which led to a southwest-directed sweep of Eocene-Oligocene volcanism across the central MCC belt (Copeland et al., 2017; Humphreys, 1995) that temporally and spatially correlated with MCC exhumation (e.g., Konstantinou et al., 2012; Zuza and Cao, 2023). Regional extension and brittle detachment faulting appears to have migrated northward from southern NV (ca. 20 Ma) to northwest Utah (<13 Ma) following the northward migration of the Mendocino triple junction (Colgan and Henry, 2009; Konstantinou et al., 2012; Zuza and Cao, 2023). These differing age trends caused by differing plate-boundary events explains the apparent decoupling between ductile shear fabrics and brittle extensional features. Therefore, we interpret that these age trends are more supportive of the buoyant diapirism model for MCC formation, especially in the context of the general shear observations reported in this study. However, we acknowledge this is still an unresolved issue, and our datasets may alternatively support the ductile attenuation and coupled detachment fault model (Fig. 2B).

The evolution of the southern MCC belt is more equivocal. These MCCs are typically interpreted as forming due to simple-shear-dominated detachment faulting (Davis, 1983; Wernicke and Axen, 1988). Here, volcanism, ductile shearing, and regional extension occur on overlapping timescales, which makes disentangling their relative contributions challenging. The greater pure shear percentage for the central MCCs (62 %) than the southern MCCs (47 %) may not be statistically significant (Fig. 5C), but it could suggest that the southern MCCs reflect a more hybrid style of MCC generation.

If the North American Cordillera MCCs are interpreted to have formed as buoyant domes, there are some important implications. First, this implies significant vertical advection of the middle-lower crust without requiring, and thus decoupled from, significant horizontal extension (Fig. 2). Ductile structures in the MCCs do not necessarily relate to the initiation of regional extension. Estimates of the magnitude of regional extension across the Basin and Range are reduced if mid-crust exhumation is caused by local instabilities and not regional normal faulting. The detachment faults in the central MCCs perplexingly

do not involve significant stratigraphic omission (Miller et al., 1983; Zuza and Dee, 2023), which was problematic for models that invoked significant extension (Wernicke, 1981) but could simply reflect the faults slipping along a flat. Continent-scale reconstructions assume significant crustal stretching (>200 % strain) around the MCCs, which is propagated into reconstructions of pre-extensional crustal thickness (e.g., Bahadori et al., 2018). However, some field workers infer less extension around the MCCs (Miller et al., 1983; Zuza and Dee, 2023), which would lead to differing reconstructions. Paleogene mid-crust diapirism that was later reactivated by Miocene moderate-magnitude extension can explain these discrepancies. Finally, a gneiss dome model for the Cordilleran MCCs implies a more generic process of crustal diapirism that is similar to other orogenic gneiss domes (Whitney et al., 2004), such as in the Himalaya (e.g., Wagner et al., 2010). Our results support that Cordilleran MCCs and gneiss domes share a similar formational mechanism that does not require regional extension and crustal thinning.

Kinematic vorticity data from other MCCs globally is limited, but a detailed study from a MCC system in North China yielded W_k values of 0.04–0.58 (98–61 % pure shear) within the core of a gneiss dome complex, with local simple shear W_k values of ~0.8–1.0 (41–0 % pure shear) adjacent to the detachment faults (Zhang et al., 2023). This was interpreted to demonstrate how simple shear fabrics related to detachment faulting may overprint earlier pure shear fabrics related to buoyant doming. The bimodal distribution of W_k values in the Cordillera compilation (Fig. 5D) may reflect combined influence of simple-shear shear zones overprinting buoyant doming.

6.3. *Kinematic vorticity analyses to interpret geologic processes*

Our analyses suggest that hot, buoyant diapirism results in characteristic wallrock pure shear strain. The rise and dipairic emplacement of

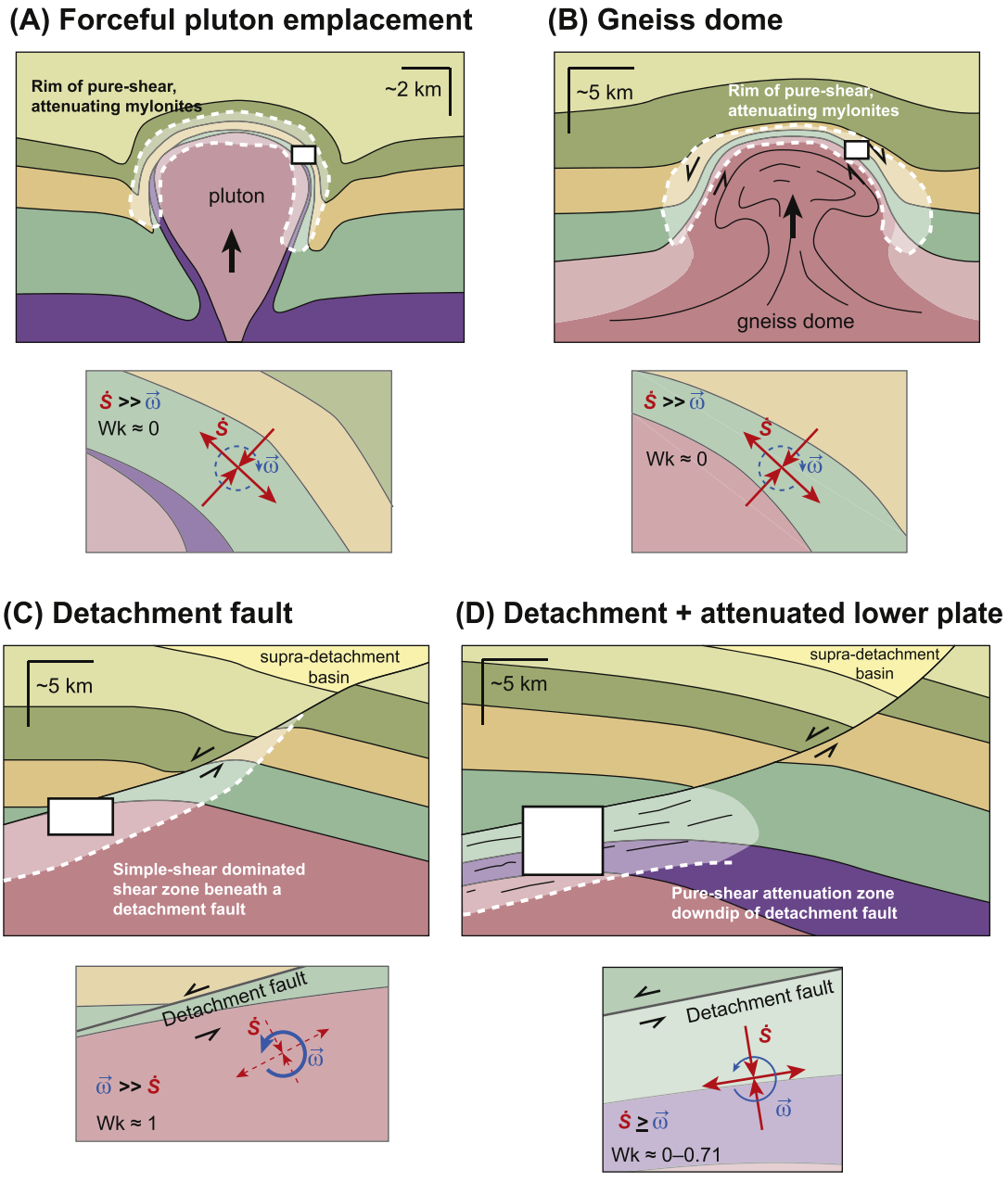

Fig. 9. Summary figure of results from this study, showing rotational flow ($\vec{\omega}$) versus stretching strain ($\dot{S}$) in shear zones associated with (A) forceful pluton emplacement, (B) gneiss dome diapirism, (C) extension with detachment faulting, and (D) detachment faulting coupled with pure shear attenuation of the lower plate.

a pluton represents a simple end-member of this process. The Papoose Flat pluton observations reveal >78 % pure shear strain and ~90 % wallrock attenuation. Another classic pluton-emplacement structure is observed around the Cretaceous Fanghsan pluton, China, where wallrock stratigraphy is attenuated ~85 % (Fig. 3B) (He et al., 2009). Kinematic vorticity analyses from this pluton reveal predominately pure shear strain (Zhao and Cong, 2014). Therefore, buoyant diapirism exemplified by pluton emplacement appears to result in bulk shear zone attenuation and pure shear strain, which matches our numerical simulations (Fig. 6). MCC generation results in similar strain characteristics, including wallrock attenuation (>80 %) (Fig. 3B) and general-shear vorticity (Figs. 5 and 9). Conversely, detachment-fault kinematics may lead to simple shear flow characteristics (Figs. 8 and 9). The buoyant ascent of the mid-crust or hot plutons may uniquely generate pure-to-general-shear fabrics due to the combined impacts of crustal heating to enable rock flow and negligible simple shear strain imparted by the rising diapir (e.g., Burov et al., 2003) (Fig. 9). Conversely, detachment-style shear zones driven by horizontal stretching of the crust and significant hanging translation relative to the footwall leads to simple shear strain (Fig. 9).

Buoyant doming is common in a variety of tectonic settings (e.g., pluton emplacement, salt domes, dome-and-keel, gneiss domes). Here we suggest that kinematic vorticity analysis of such shear zones may be a diagnostic tool for their interpretation, in addition to traditional geologic mapping and pressure-temperature-time (*P-T-t*) evaluation. For example, Himalayan gneiss domes have previously been interpreted to have formed via contractional duplexing, large-scale normal faulting, or buoyant doming. However, kinematic vorticity analysis of Himalayan domes reveals general shear strain characteristics (48–69 % pure shear) that may imply buoyant doming that was synchronous with partial melting across the Himalaya (Wagner et al., 2010). This kinematic and dynamic interpretation would match Cordillera MCCs as discussed in this study.

Another example is the debate between vertical versus horizontal tectonics in Early Earth (Kusky et al., 2021; Webb et al., 2020), where dome-and-keel structures are interpreted as either buoyancy instabilities (Van Kranendonk et al., 2007) or heavily modified plate-tectonic (e.g., paleo-horizontal kinematics) features (e.g., Kloppenburg et al., 2001). We suggest that analysis of these ancient shear zones (Zuo et al., 2021) to compare against modern analogs such as buoyant diapirs or pluton-emplacement structures, may provide important insights.

6.4. Limitations and future directions

There are strengths and weaknesses of the various W_k methods (e.g., Xypolias, 2010), but we argue that the approach presented in this study provides an unbiased way to examine shear zone samples and compare results between different geologic provinces. Our approach using the supplied MATLAB script reduces user bias in selecting and outlining recrystallized grains or porphyroblasts. The δ-β method works with fine-grained recrystallized rock types that are common in many shear zones, without relying on large porphyroblasts (e.g., RGN) or relict phases for finite-strain analysis (e.g., R_{xz}-β).

A limitation of most vorticity methods is that they only consider a 2D flow pattern viewed within the VNS. Here we assumed 2D plane strain, which may overestimate W_k compared to a complete 3D vorticity flow field, but this overestimation is likely small (<0.05 W_k) (Tikoff and Fossen, 1995; Xypolias, 2010). Furthermore, we provide a metric to ensure that the W_k estimate is in the correct VNS reference frame through CVA analyses and the C_Y parameter.

Our numerical simulations calculated a bulk vorticity at every given model node, which may oversimplify shear-zone kinematics adjacent to relatively undeformed wallrock. Ductile shear zones operate primarily on the cm- to km- scale, and therefore individual shear-zone kinematics may differ from bulk vorticity estimated in these models. Furthermore, W_k observed in a sample is the internal kinematic vorticity, which does not reflect any external kinematics, such as rigid body rotation or translation. The models cannot completely deconvolve large-scale rotation from sample-scale vorticity. However, our approach of ignoring super simple shear ($W_k > 1$) and regions of low strain rate allows us to predict patterns of W_k that may be transferable to observed rock samples.

Vorticity-enhanced accessory phase petrochronology can provide a robust way to date ductile shear zones. Specifically, if deformation-induced dislocation creep can reset a U-Pb age (e.g., Gordon et al., 2021; Moser et al., 2022; Odlum et al., 2022) and this deformation can be kinematically linked to the bulk fabric forming event via CVA analyses (Miranda et al., 2023), one could extract reliable ages that are directly tied to a unique deformational event. This approach can help resolve multiple phases of deformation in complex settings. Here we have presented a method to quantify the relationship of the CVA with the sample Y axis (i.e., C_Y), and we suggest that future vorticity-based petrochronology efforts may similarly use this parameter to compare bulk and single-phase CVA axes to confirm similar kinematic conditions.

7. Conclusions

The kinematic vorticity of a shear zone may characteristically reflect its formation mechanisms. We sought to test the hypothesis that North American Cordillera MCCs formed due to buoyant diapirism by determining W_k values from four distinct MCC systems and an analogous forcefully emplaced pluton. We introduce a method of W_k determination that incorporates high-resolution EBSD maps and the methods of Wallis (1995). Most of the analyzed samples displayed a mix of pure- and simple-shear kinematics (average 70 % pure shear). The significant component of pure shear strain is consistent with observations of bulk vertical shortening required by the attenuation of sedimentary rocks involved within the shear zones (~90 % vertical shortening). Numerical simulations of the W_k field confirm that buoyant diapirs lead to pure shear dominated deformation, whereas discrete normal-faulting alone leads to more simple shear.

We argue that buoyant diapirism was important for MCC generation, and these shear zones do not merely reflect simple shear strain due to major detachment faulting. As the middle crust buoyantly upwells, flanking shear zones are strongly attenuated leading to general-shear strain. This process may be analogous to diapiric pluton emplacement. We suggest our kinematic vorticity method may be used to test other tectonic processes where buoyant diapirism versus horizontal faulting is debated, such as debates regarding dome-and-keel versus plate tectonics in the Archean.

CRediT authorship contribution statement

Andrew V. Zuza: Writing – original draft, Visualization, Supervision, Software, Methodology, Investigation, Funding acquisition, Formal analysis, Data curation, Conceptualization. **Wenrong Cao:** Writing – review & editing, Software, Methodology, Formal analysis, Conceptualization. **Drew A. Levy:** Writing – review & editing, Methodology. **Joel W. DesOrmeau:** Writing – review & editing, Methodology. **Margaret L. Odlum:** Writing – review & editing, Methodology, Investigation. **Andrew A. Siciliano:** Writing – review & editing, Investigation.

Declaration of competing interest

The authors declare that they have no known competing financial interests or personal relationships that could have appeared to influence the work reported in this paper.

Data availability

Data will be made available on request.

Acknowledgements

This work was partially supported by the U.S. Geological Survey National Cooperative Geologic Mapping Program via STATEMAP awards (G19AC00383, G20AS00006) and the National Science Foundation Tectonics program (EAR 1830139, EAR 2221618). We thank Editor Alex Webb for efficient editorial handling, and Sean Long and an anonymous reviewer for constructive comments that clarified our work.

Supplementary materials

Supplementary material associated with this article can be found, in the online version, at doi:10.1016/j.epsl.2024.118964.

References

Armstrong, R., Ward, P., 1991. Evolving geographic patterns of Cenozoic magmatism in the North American Cordillera: The temporal and spatial association of magmatism and metamorphic core complexes. J. Geophys. Res.: Solid. Earth.

Bahadori, A., Holt, W.E., Rasbury, E.T., 2018. Reconstruction modeling of crustal thickness and paleotopography of western North America since 36 Ma. Geosphere 14, 1207–1231. https://doi.org/10.1130/GES01604.1.

Bartley, J.M., Wernicke, B.P., 1984. The Snake Range Décollement interpreted as a major extensional shear zone. Tectonics 3, 647–657. https://doi.org/10.1029/TC003i006p00647.

Burov, E., Jaupart, C., Guillou-Frottier, L., 2003. Ascent and emplacement of buoyant magma bodies in brittle-ductile upper crust. J. Geophys. Res.: Solid Earth 108. https://doi.org/10.1029/2002JB001904.

Bykerk-Kauffman, A., Janecke, S.U., 1987. Late Cretaceous to early Tertiary ductile deformation: Catalina-Rincon metamorphic core complex, southeastern Arizona. Geology 15, 462–465. https://doi.org/10.1130/0091-7613(1987)15<462:LCTETD>2.0.CO;2.

Colgan, J.P., Henry, C.D., 2009. Rapid middle miocene collapse of the mesozoic orogenic plateau in north-central nevada. Int. Geol. Rev. 51, 920–961. https://doi.org/10.1080/00206810903056731.

Coney, P.J., 1980. Cordilleran metamorphic core complexes: An overview. In: Crittenden, M.D., Coney, P.J., Davis, G.H. (Eds.), Cordilleran Metamorphic Core Complexes, 153. Geological Society of America Memoir, pp. 7–34.

Copeland, P., Currie, C.A., Lawton, T.F., Murphy, M.A., 2017. Location, location, location: the variable lifespan of the Laramide orogeny. Geology 45, 223–226. https://doi.org/10.1130/G38810.1.

Davis, G.H., 1983. Shear-zone model for the origin of metamorphic core complexes. Geology 11, 342–347. https://doi.org/10.1130/0091-7613(1983)11<342:SMFTOO>2.0.CO;2.

de Saint-Blanquat, M., Law, R.D., Bouchez, J.-L., Morgan, S.S., 2001. Internal structure and emplacement of the papoose flat pluton: an integrated structural, petrographic, and magnetic susceptibility study. GSA Bulletin 113, 976–995. https://doi.org/10.1130/0016-7606(2001)113<0976:ISAEOT>2.0.CO;2.

Dell'angelo, L.N., Tullis, J., 1989. Fabric development in experimentally sheared quartzites. Tectonophysics 169, 1–21. https://doi.org/10.1016/0040-1951(89)90180-7.

Díaz-Azpiroz, M., Fernández, C., Czeck, D.M., 2019. Are we studying deformed rocks in the right sections? Best practices in the kinematic analysis of 3D deformation zones. J. Struct. Geology, Back to the future 125, 218–225. https://doi.org/10.1016/j.jsg.2018.03.005.

Erskine, B.G., Heidelbach, F., Wenk, H.-R., 1993. Lattice preferred orientations and microstructures of deformed Cordilleran marbles: correlation of shear indicators and determination of strain path. J. Struct. Geol. 15, 1189–1205. https://doi.org/10.1016/0191-8141(93)90163-5.

Eskola, P.E., 1948. The problem of mantled gneiss domes. Quarterly J. Geolog. Society 104, 461–476. https://doi.org/10.1144/GSL.JGS.1948.104.01-04.21.

Faleiros, F.M., Moraes, R., Pavan, M., Campanha, G.A.C., 2016. A new empirical calibration of the quartz c-axis fabric opening-angle deformation thermometer. Tectonophysics 671, 173–182. https://doi.org/10.1016/j.tecto.2016.01.014.

Fossen, H., Cavalcante, G.C.G., 2017. Shear zones – A review. Earth Sci. Rev. 171, 434–455. https://doi.org/10.1016/j.earscirev.2017.05.002.

Gans, P., Mahood, G., Schermer, E., 1989. Synextensional Magmatism in the Basin and Range Province; A case Study from the Eastern Great Basin. Geological Society of America Special Papers. Geological Society of America. https://doi.org/10.1130/SPE233.

Gordon, S.M., Kirkland, C.L., Reddy, S.M., Blatchford, H.J., Whitney, D.L., Teyssier, C., Evans, N.J., McDonald, B.J., 2021. Deformation-enhanced recrystallization of titanite drives decoupling between U-Pb and trace elements. Earth Planet. Sci. Lett. 560, 116810 https://doi.org/10.1016/j.epsl.2021.116810.

He, B., Xu, Y.-G., Paterson, S., 2009. Magmatic diapirism of the Fangshan pluton, southwest of Beijing. China. J. Struct. Geol. 31, 615–626. https://doi.org/10.1016/j.jsg.2009.04.007.

Henry, C.D., McGrew, A.J., Colgan, J.P., Snoke, A.W., Brueseke, M.E., 2011. Timing, distribution, amount, and style of Cenozoic extension in the northern Great Basin. Geologic Field Trips to the Basin and Range, Rocky Mountains, Snake River Plain, and Terranes of the U.S. Cordillera. Geological Society of America, pp. 27–66. https://doi.org/10.1130/2011.0021(02.

Humphreys, E.D., 1995. Post-Laramide removal of the Farallon slab, western United States. Geol 23, 987. https://doi.org/10.1130/0091-7613(1995)023<0987:PLROTF>2.3.CO;2.

Kaus, B.J.P., 2010. Factors that control the angle of shear bands in geodynamic numerical models of brittle deformation. Tectonophysics, Quantitative modell. Geolog. Processes 484, 36–47. https://doi.org/10.1016/j.tecto.2009.08.042.

Kloppenburg, A., White, S.H., Zegers, T.E., 2001. Structural evolution of the Warrawoona Greenstone Belt and adjoining granitoid complexes, Pilbara Craton, Australia: implications for Archaean tectonic processes. Precambrian Res. 112, 107–147. https://doi.org/10.1016/S0301-9268(01)00172-3.

Konstantinou, A., Strickland, A., Miller, E.L., Wooden, J.P., 2012. Multistage cenozoic extension of the Albion–Raft River–Grouse creek metamorphic core complex: Geochronologic and stratigraphic constraints. Geosphere 8, 1429–1466. https://doi.org/10.1130/GES00778.1.

Kusky, T., Windley, B.F., Polat, A., Wang, L., Ning, W., Zhong, Y., 2021. Archean dome-and-basin style structures form during growth and death of intraoceanic and continental margin arcs in accretionary orogens. Earth Sci. Rev. 220, 103725 https://doi.org/10.1016/j.earscirev.2021.103725.

Law, R.D., Searle, M.P., Simpson, R.L., 2004. Strain, deformation temperatures and vorticity of flow at the top of the Greater himalayan slab, everest massif, Tibet. JGS 161, 305–320. https://doi.org/10.1144/0016-764903-047.

Lee, J., Blackburn, T., Johnston, S., 2017. Timing of mid-crustal ductile extension in the northern Snake Range metamorphic core complex, Nevada: Evidence from U/Pb zircon ages. Geosphere 13, 439–459. https://doi.org/10.1130/GES01429.1.

Lee, J., Miller, E.L., Sutter, J.F., 1987. Ductile Strain and Metamorphism in an Extensional Tectonic setting: a Case Study from the Northern Snake Range, Nevada, USA, 28. Special Publications, Geological Society, London, pp. 267–298. https://doi.org/10.1144/GSL.SP.1987.028.01.18.

Levy, D.A., Zuza, A.V., Michels, Z.D., DesOrmeau, J.W., 2023. Buoyant doming generates metamorphic core complexes in the North American Cordillera. Geology 51, 290–294. https://doi.org/10.1130/G50752.1.

Lister, G.S., Davis, G.A., 1989. The origin of metamorphic core complexes and detachment faults formed during Tertiary continental extension in the northern Colorado River region, U.S.A. J. Struct. Geol. 11, 65–94. https://doi.org/10.1016/0191-8141(89)90036-9.

Long, S.P., Gordon, S.M., Young, J.P., Soignard, E., 2016. Temperature and strain gradients through Lesser Himalayan rocks and across the Main Central thrust, south central Bhutan: Implications for transport-parallel stretching and inverted metamorphism. Tectonics 35, 1863–1891. https://doi.org/10.1002/2016TC004242.

Long, S.P., Lee, J., Blackford, N.R., 2023. Extreme ductile thinning of cambrian marbles in the northern snake range metamorphic core complex, Nevada, USA: Implications for extension magnitude and structural evolution. J. Struct. Geol. 173, 104912 https://doi.org/10.1016/j.jsg.2023.104912.

Long, S.P., Mullady, C.L., Starnes, J.K., Gordon, S.M., Larson, K.P., Pianowski, L.S., Miller, R.B., Soignard, E., 2019. A structural model for the South Tibetan detachment system in northwestern Bhutan from integration of temperature, fabric, strain, and kinematic data. Lithosphere 11, 465–487. https://doi.org/10.1130/L1049.1.

Martinez, F., Goodliffe, A.M., Taylor, B., 2001. Metamorphic core complex formation by density inversion and lower-crust extrusion. Nature 411, 930–934. https://doi.org/10.1038/35082042.

McFadden, R.R., Shroeder, H., Johnson, I., Teyssier, C., Taylor, J., Seaton, N., Gilman, B., 2020. Vorticity and Microstructural Analysis of the Wildhorse Detachment in the Pioneer metamorphic Core complex, Idaho. Presented at the GSA 2020 Connects Online. GSA.

Means, W.D., Hobbs, B.E., Lister, G.S., Williams, P.F., 1980. Vorticity and non-coaxiality in progressive deformations. J. Struct. Geol. 2, 371–378. https://doi.org/10.1016/0191-8141(80)90024-3.

Michels, Z.D., Kruckenberg, S.C., Davis, J.R., Tikoff, B., 2015. Determining vorticity axes from grain-scale dispersion of crystallographic orientations. Geology 43, 803–806. https://doi.org/10.1130/G36868.1.

Miller, E.L., Gans, P.B., Garing, J., 1983. The snake range décollement: an exhumed Mid-Tertiary ductile-brittle transition. Tectonics 2, 239–263. https://doi.org/10.1029/TC002i003p00239.

Miranda, E.A., Brown, V., Schwartz, J.J., Klepeis, K.A., 2023. Making sense of shear zone fabrics that record multiple episodes of deformation: Electron backscatter diffraction–derived and crystallographic vorticity axis–enhanced petrochronology. Geology 51, 591–596. https://doi.org/10.1130/G50982.1.

Moser, A.C., Hacker, B.R., Gehrels, G.E., Seward, G.G.E., Kylander-Clark, A.R.C., Garber, J.M., 2022. Linking titanite U–Pb dates to coupled deformation and dissolution–reprecipitation. Contrib. Mineral. Petrol. 177, 42. https://doi.org/10.1007/s00410-022-01906-9.

Odlum, M.L., Levy, D.A., Stockli, D.F., Stockli, L.D., DesOrmeau, J.W., 2022. Deformation and metasomatism recorded by single-grain apatite petrochronology. Geology 50, 697–703. https://doi.org/10.1130/G49809.1.

Ranalli, G., 1995. Rheology of the Earth. Springer Science & Business Media.

Rey, P.F., Teyssier, C., Whitney, D.L., 2009. The role of partial melting and extensional strain rates in the development of metamorphic core complexes. Tectonophysics, Hot orogens 477, 135–144. https://doi.org/10.1016/j.tecto.2009.03.010.

Singleton, J.S., 2011. Kinematic and Geometric Evolution of the Buckskin-Rawhide metamorphic Core complex, West-Central Arizona. The University of Texas at Austin, Austin, Texas.

Singleton, J.S., Wong, M.S., Johnston, S.M., 2018. The role of calcite-rich metasedimentary mylonites in localizing detachment fault strain and influencing the

structural evolution of the Buckskin-Rawhide metamorphic core complex, west-central Arizona. Lithosphere 10, 172–193. https://doi.org/10.1130/L699.1.
Snoke, A.W., 1980. Transition from Infrastructure to Suprastructure in the Northern Ruby Mountains. Nevada. https://doi.org/10.1130/MEM153-p287.
Spencer, J.E., Richard, S.M., Bykerk-Kauffman, A., Constenius, K.N., Valencia, V.A., 2022. Structure, chronology, kinematics, and geodynamics of tectonic extension in the greater Catalina metamorphic core complex, southeastern Arizona, USA. Geosphere 18, 1643–1678. https://doi.org/10.1130/GES02485.1.
Sullivan, W.A., 2008. Significance of transport-parallel strain variations in part of the Raft River shear zone, Raft River Mountains, Utah, USA. J. Struct. Geol. 30, 138–158. https://doi.org/10.1016/j.jsg.2007.11.007.
Sylvester, A.G., Ortel, G., Nelson, C.A., Christie, J.M., 1978. Papoose flat pluton: a granitic blister in the Inyo Mountains. California. Geol Soc America Bull 89, 1205. https://doi.org/10.1130/0016-7606(1978)89<1205:PFPAGB>2.0.CO;2.
Tikoff, B., Fossen, H., 1995. The limitations of three-dimensional kinematic vorticity analysis. J. Struct. Geol. 17, 1771–1784. https://doi.org/10.1016/0191-8141(95)00069-P.
Tirel, C., Brun, J.-P., Burov, E., 2008. Dynamics and structural development of metamorphic core complexes. J. Geophys. Res.: Solid Earth 113. https://doi.org/10.1029/2005JB003694.
Truesdell, C., 1953. Two Measures of Vorticity. Indiana Univ. Math. J. 2, 173–217. https://doi.org/10.1512/iumj.1953.2.52009.
Van Kranendonk, M.J., Hugh Smithies, R., Hickman, A.H., Champion, D.c., 2007. Review: secular tectonic evolution of Archean continental crust: interplay between horizontal and vertical processes in the formation of the Pilbara Craton. Australia. Terra Nova 19, 1–38. https://doi.org/10.1111/j.1365-3121.2006.00723.x.
Wagner, T., Lee, J., Hacker, B.R., Seward, G., 2010. Kinematics and vorticity in Kangmar Dome, southern Tibet: Testing midcrustal channel flow models for the Himalaya. Tectonics 29. https://doi.org/10.1029/2010TC002746.
Wallis, S., 1995. Vorticity analysis and recognition of ductile extension in the Sanbagawa belt. SW Japan. J. Struct. Geology 17, 1077–1093. https://doi.org/10.1016/0191-8141(95)00005-X.
Webb, A.A.G., Müller, T., Zuo, J., Haproff, P.J., Ramírez-Salazar, A., 2020. A non–plate tectonic model for the Eoarchean Isua supracrustal belt. Lithosphere 12, 166–179. https://doi.org/10.1130/L1130.1.
Wells, M.L., 2001. Rheological control on the initial geometry of the Raft River detachment fault and shear zone, western United States. Tectonics 20, 435–457. https://doi.org/10.1029/2000TC001202.
Wenk, H.-R., Takeshita, T., Bechler, E., Erskine, B.G., Matthies, S., 1987. Pure shear and simple shear calcite textures. Comparison of experimental, theoretical and natural data. J. Struct. Geol. 9, 731–745. https://doi.org/10.1016/0191-8141(87)90156-8.
Wernicke, B., 1981. Low-angle normal faults in the Basin and Range Province: nappe tectonics in an extending orogen. Nature 291, 645–648. https://doi.org/10.1038/291645a0.
Wernicke, B., Axen, G.J., 1988. On the role of isostasy in the evolution of normal fault systems. Geology 16, 848–851. https://doi.org/10.1130/0091-7613(1988)016<0848:OTROII>2.3.CO;2.
Whitney, D., Teyssier, C., Siddoway, C.S., 2004. Gneiss Domes in Orogeny. Geological Society of America.
Whitney, D.L., Teyssier, C., Rey, P., Buck, W.R., 2013. Continental and oceanic core complexes. GSA Bulletin 125, 273–298. https://doi.org/10.1130/B30754.1.
Xypolias, P., 2010. Vorticity analysis in shear zones: a review of methods and applications. J. Structural Geology, Struct. Diagenesis 32, 2072–2092. https://doi.org/10.1016/j.jsg.2010.08.009.
Yun, S., 2018. Mechanical Analysis of a Detachment Shear Zone, Picacho Mountains Metamorphic Core Complex (AZ) (M.S.). University of Louisiana at Lafayette, United States – Louisiana.
Zhang, Y., Dong, S., Shi, W., 2023. Hot thermal upwelling-extensional structure: Recognition of “metamorphic core complexes” in North China. Chin. Sci. Bull. https://doi.org/10.1360/TB-2023-0402.
Zhao, N., Jr., Cong, F., 2014. Microstructural Characteristics and Deformation Mechanism of the Shear Zone of Fangshan Pluton, North China.
Zuo, J., Webb, A.A.G., Piazolo, S., Wang, Q., Müller, T., Ramírez-Salazar, A., Haproff, P. J., 2021. Tectonics of the isua supracrustal belt 2: microstructures reveal distributed strain in the absence of major fault structures. Tectonics 40, e2020TC006514. https://doi.org/10.1029/2020TC006514.
Zuza, A., Cao, W., 2023. Metamorphic core complex dichotomy in the north american cordillera explained by buoyant upwelling in variably thick crust. GSAT 33, 4–11. https://doi.org/10.1130/GSATG548A.1.
Zuza, A.V., Dee, S., 2023. Decoupled Oligocene mylonitic shearing and Miocene detachment faulting in the East Humboldt Range metamorphic core complex, northeast Nevada, USA. Geosphere 19, 1318–1347. https://doi.org/10.1130/GES02619.1.
Zuza, A.V., Levy, D.A., Dee, S., DesOrmeau, J.W., Cheng, F., Li, X., 2022. Structural architecture and attenuation of the ductile lower plate of the ruby mountain-east humboldt range metamorphic core complex, northeast Nevada. Tectonics 41, e2021TC007162. https://doi.org/10.1029/2021TC007162.